Nearly complete segregation of submerged grains in a rotating drum

Yu Chen [1], Deheng Wei [1,2,*], Si Suo [3], Mingrui Dong [1], and Yixiang Gan [1,†]
[1]*School of Civil Engineering, The University of Sydney, Sydney, Australia*
[2]*State Key Laboratory of Intelligent Deep Metal Mining and Equipment, School of Resources and Civil Engineering, Northeastern University, Shenyang 110819, China*
[3]*Department of Civil and Environmental Engineering, Imperial College London, London, United Kingdom*

(Received 20 February 2025; accepted 4 June 2025; published 24 June 2025)

Density-driven segregation, extensively studied in a simple rotating drum, is enriched with a wide range of underlying physics. Diverse symmetrical segregation patterns formed by mixing two types of dry mono-sized grains have been revealed due to variations in heavy and light grain densities ρ_h and ρ_l and rotating speeds ω. We engender experimentally a nearly complete segregation, not occurring in dry conditions of the same ρ_h, ρ_l, and ω, in submerged states. Furthermore, based on the experiment-validated simulations, using coupled computational fluid dynamics and the discrete element method, it is found the mixing index can be well predicted over a wide parameter space in the effective density ratio, $\mathcal{D} = (\rho_h - \rho_f)/(\rho_l - \rho_f)$ with ρ_f being the fluid density. Specifically, with increasing $\mathcal{D}$ well-mixed states transit to fully segregated states with a rising number of vortices and more severe asymmetrical patterns. When the global Reynolds number Re_g is enlarged, the vortex area of heavy particles shrinks for lower $\mathcal{D}$, while the area of light particles gradually saturates; meanwhile, for higher $\mathcal{D}$ a new vortex with a continuously expanded area can be encountered in the light particle zone. These results improve our understanding of segregation transitions, especially in submerged granular systems, and shed new light on various science and engineering practices.

DOI: 10.1103/kjhc-9chw

I. INTRODUCTION

Understanding granular segregation is of vital importance in many geophysical problems and industrial applications, ranging from sediment transport [1,2] to mixing processes in pharmaceutical and wood pulp engineering [3,4]. Granular materials often exhibit spontaneous segregation based on differences in size, shape, and density, leading to distinct phase separations [5]. Proceeding from the minimal case of mixing two types of spherical grains in a thin rotating cylindrical container, the chaotic mixing and segregation in dry granular flows are well studied on density-dispersity in mono-sized particles (D-system) and size-dispersity in grains of the same density (S-system), where the types of grains in each system are identical. In the former, "central core" patterns of heavy grains sunk into light grains could be formed in the symmetrical mixtures [6–8], due to the buoyancy-driven mechanism [9–11]. Such a symmetry, induced by high grain density, $\mathfrak{D} = \rho_h/\rho_l$, might hinder the postmortem de-mixing by potential re-mixing. This can be alleviated by rotating the two binary density grains in submerged conditions [12], wherein it is observed that the central core moves downward along the inclined slope. Inspired by the effects of interstitial fluids

*Contact author: deheng.wei@sydney.edu.au
†Contact author: yixiang.gan@sydney.edu.au

on a density disperse system, we aim to tackle a nearly complete segregation with the central core clustering near the drum boundary.

In this light, it is surprising that so little attention has been paid to quantifying the segregation efficiency of wet rotating drums. One of the main reasons for this is that the particle-fluid interaction force is inherently difficult to measure, unlike the particle-particle contact force; the intriguing, yet dominant parts of it (i.e., drag and lift forces) are scaled with the root of the relative velocity [13]. To date, the velocity-dependent drag and lift coefficients can only be determined indirectly, by more or less empirical fits [14]. Considering the high-velocity gradient in a drum to attain high grain segregation intensity, the configuration is too experimentally complicated to delineate the quantitative influences of each fluid property. The numerical modelling is therefore an effective candidate to isolate the effect of focused factors, such as the effective density ratio $\mathcal{D} = (\rho_h - \rho_f)/(\rho_l - \rho_f)$ in this study, from other dominants, on critical metrics quantifying grain segregation.

Numerous experimental and numerical investigations have been conducted on the dry granular segregation in density-disperse systems. The mixing efficiency of binary grain mixtures has been frequently measured by the mixing index, first proposed by Lacey [15]. By tracking trajectories of the heavier particles in a quasi-two-dimensional (quasi-2D) drum experimentally, Ristow [16] quantified the segregation rate and its dependence on the dry particle density ratio $\mathfrak{D}$ at a cascading regime. Khakhar, McCarthy, and Ottino [17] further demonstrated that the composition profiles of heavy and light grains remained independent of the level of particle filling. Using numerical simulations based on the distinct element method (DEM), the settling dynamics of a single high-density particle within a granular mixture illustrates that the motion of the high-density tracer is characterized by the "segregation force," combining with grain-grain buoyancy and drag forces [18].

Buoyancy-driven segregation of dry grains often engenders the formation of distinct layers, observed in both vibrated granular mixtures [19,20] and rotating drums [21,22]. Lighter particles migrate towards the periphery and form a segregated layer, leading to stratified configurations. These regimes include rolling and cascading regimes, with an elliptical vortex observed at the core of the flow and highly overlapping with the convection roll cores of heavier particulates [23]. Much attention has been paid to identifying the only vortex in a dry density disperse system by tracking streamlines to determine its location and area [24–26]. How the vortex in submerged density disperse system evolves by the combined effects of $\mathcal{D}$ and ω deserves, at least, equal attention.

In this work, we aim to investigate the nearly complete segregation behavior of submerged binary-mixed grains in a rotating drum. We employ a combined experimental and numerical method to systematically explore how the effective density ratio and rotating speed influence segregation patterns. We identify four different states of mixing, ranging from homogeneous mixing to the development of distinct segregated regions through the formation of multiple vortices. Corresponding mixing states transition from well-mixed to nearly complete segregation state is influenced by the effective density ratio, irrespective of fluid density, and characterized by the mixing index; further transitions in nearly complete segregated stages are highly sensitive to both the effective density ratio and the rotating speed. By gaining a deeper understanding of these segregation states, this research provides a clearer picture of nearly complete segregation processes in a submerged density-disperse system within a rotating drum.

II. METHODOLOGY

A. Experimental configuration

Figure 1(a) shows our experimental setup, consisting of a drum container with an inner diameter of 150 mm and a thickness of 30 mm. The drum is driven by a high-torque stepper rotator controlled by a rotating controller, providing rotating speed within [5,60] rpm. The relatively narrow width was selected to minimize axial segregation [27,28] and ensure that the observed dynamics primarily reflect radial segregation. The mixtures were composed of binary spherical particles with different

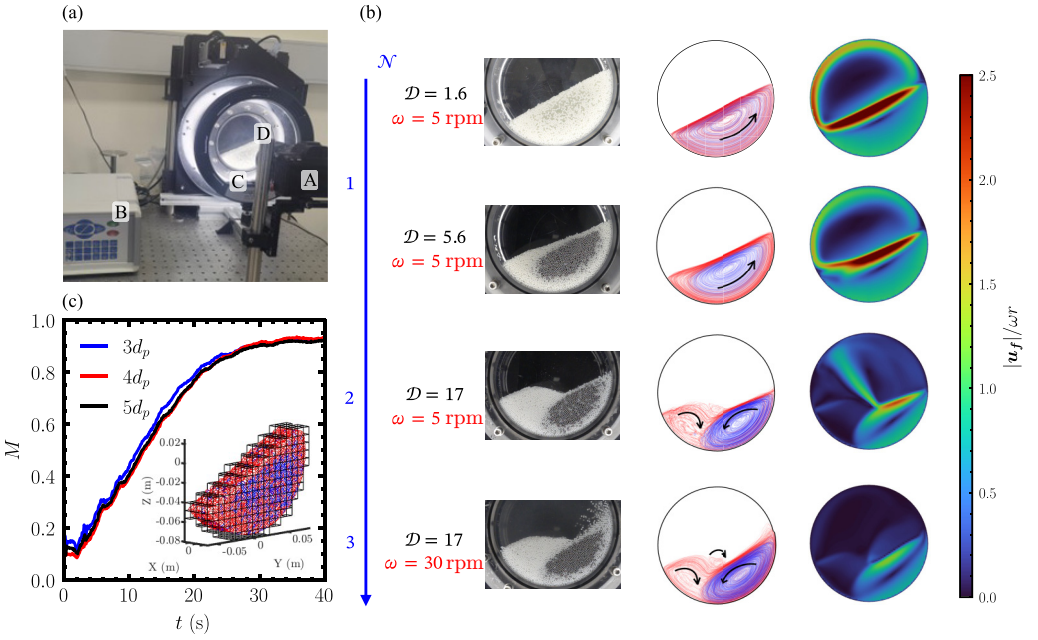

FIG. 1. (a) Experimental setup: A, B, C, and D are the camera, rotating controller, light system, and counterclockwise-rotated thin cylindrical container, respectively. (b) Flow patterns observed at various $\mathcal{D} = (\rho_h - \rho_f)/(\rho_l - \rho_f)$ and ω, and $\mathcal{N}$denotes the number of vortices. The left column displays the experimental observations; while the middle column illustrates the particle trajectories derived from the corresponding numerical simulations, with arrows indicating the direction of vortex rotation; and the right column presents the magnitude of the fluid velocity field $|\boldsymbol{u}_f|$, normalized by the tangential speed ωr, where r is the drum radius. In the middle column, the trace colors red and blue are for light and heavy grains, respectively. (c) Sensitivity study of the Lacey mixing index M with respect to different grid size ℓ over time for the case $\mathcal{D} = 1.6$ and $\omega = 5$ rpm. The inset shows the grids used in the M calculation with $\ell = 4d_p$; the coordinate (0,0) corresponds to the center of the drum.

densities selected from three materials: polyoxymethylene (POM, $\rho_{s,\mathrm{POM}} = 1382\ \mathrm{kg/m^3}$), glass beads ($\rho_{s,\mathrm{glass}} = 2363\ \mathrm{kg/m^3}$), and stainless steel ($\rho_{s,\mathrm{steel}} = 7803\ \mathrm{kg/m^3}$). All of them have the same nominal diameter d_p of 2 mm ± 3%. The initial mixtures were prepared with an equal number of 14 274 particles of the two selected types. The corresponding packing fraction was approximately 0.62; and the filling ratio, defined as the ratio of the total filled volume to the drum volume, was about 0.356. In the experiment, the submerged condition referred to grains rotating in a drum fully filled with purified water whose density $\rho_w = 1000\ \mathrm{kg/m^3}$. All tests were conducted in a laboratory maintained at a room temperature of 22 °C and an atmospheric pressure of 1 atm, resulting in the water viscosity of 0.001 Pa s. The flow patterns were recorded until the steady flow state was achieved. Figure 1(b) shows flow patterns at steady state with various conditions (See videos in Supplemental Material [29]). The experimental procedures are designed to ensure repeatability, with all critical parameters—particle size distribution, packing fraction, drum filling ratio, and rotating speed—carefully controlled to minimize variability between trials. Further details of the experiment can be seen in our previous work [23].

B. Governing equations and numerical scheme

An unresolved three-dimensional (3D) CFD-DEM approach [30] is employed to simulate the dynamics in the density-disperse system, implemented using the open-source CFDEMPROJECT

library. The fluid phase is treated as a continuum and modeled in an Eulerian framework [31] using local-averaged Navier-Stokes equations:

$$\frac{\partial}{\partial t}(\varepsilon_{\mathrm{f}}\rho_{\mathrm{f}}) + \nabla\cdot(\varepsilon_{\mathrm{f}}\rho_{\mathrm{f}}\boldsymbol{u}_{\mathrm{f}}) = 0, \tag{1}$$

$$\frac{\partial}{\partial t}(\varepsilon_{\mathrm{f}}\rho_{\mathrm{f}}\boldsymbol{u}_{\mathrm{f}}) + \nabla(\varepsilon_{\mathrm{f}}\rho_{\mathrm{f}}\boldsymbol{u}_{\mathrm{f}}\boldsymbol{u}_{\mathrm{f}}) = -\varepsilon_{\mathrm{f}}\nabla p_{\mathrm{f}} + \nabla\cdot(\varepsilon_{\mathrm{f}}\mathbf{T}_{\mathrm{f}}) + \varepsilon_{\mathrm{f}}\rho_{\mathrm{f}}\boldsymbol{g} - \mathbf{F}_{pf}, \tag{2}$$

where ε_{f} is the local fluid fraction, ρ_{f} is the fluid density, $\boldsymbol{u}_{\mathrm{f}}$ is the fluid velocity, and the stress tensor $\mathbf{T}_{\mathrm{f}} = \mu_{\mathrm{f}}(\nabla\boldsymbol{u}_{\mathrm{f}} + \nabla\boldsymbol{u}_{\mathrm{f}}{}^{T})$. Other items on the right side of Eq. (2) denote the pressure gradient, gravitational force, and particle-fluid interaction force, respectively.

The particle dynamics are solved using a DEM framework, in which both translational and rotational motions are accounted for. These distinct motions are governed by the principles of Newton's second law and the angular momentum equation:

$$m_i\frac{d\boldsymbol{v}_i}{dt} = m_i\boldsymbol{g} + \boldsymbol{f}_{c,i} + \boldsymbol{f}_{pf,i}, \tag{3}$$

$$I_i\frac{d\boldsymbol{\omega}_i}{dt} = \boldsymbol{M}_i, \tag{4}$$

where m_i, $\boldsymbol{v}_i$, I_i, and $\boldsymbol{\omega}_i$ denote the mass, translational velocity, moment of inertia, and angular velocity of the ith particle, respectively. For the interparticle contact, $\boldsymbol{f}_{c,i}$ is composed of two parts, i.e., the normal force solved by the Hertzian contact model, and the tangential one governed by the finite Coulomb friction model and characterized by the friction coefficient μ_{s}. For the particle rotation, we consider a rolling resistance for calculating the total moment $\boldsymbol{M}_i$, characterized by the rolling friction coefficient μ_r. The collision energy loss by the inelasticity is considered through a restitution coefficient e in both normal and tangential directions [32,33]. For the particle-fluid interaction, $\boldsymbol{f}_{pf,i}$ includes both the Archimedes buoyancy force $\boldsymbol{f}_{b,i} = V_i(-\nabla p_{\mathrm{f}} + \nabla\cdot\mathbf{T}_{\mathrm{f}})$ and drag force $\boldsymbol{f}_{d,i} = \beta V_i(\boldsymbol{u}_{f,i} - \boldsymbol{v}_i)/(\varepsilon_{\mathrm{f}} - \varepsilon_{\mathrm{f}}{}^2)$. Herein, V_i is the volume of particle i and β is the interphase momentum exchange coefficient determined by the Gidaspow drag model [34],

$$\beta = \begin{cases} \frac{150(1-\varepsilon_f)\boldsymbol{u}_f}{\varepsilon_f d_p^2} + 1.75\frac{(1-\varepsilon_f)\rho_f|\boldsymbol{u}_f-\boldsymbol{v}_p|}{d_p} & \varepsilon_f \leqslant 0.8 \\ \frac{3}{4}\frac{\varepsilon_f(1-\varepsilon_g)\rho_f|\boldsymbol{u}_f-\boldsymbol{v}_p|}{d_p}C_D\varepsilon_f^{-2.65} & \varepsilon_f > 0.8, \end{cases} \tag{5}$$

$$C_D = \begin{cases} \frac{24}{\mathrm{Re}_p}\left(1 + 0.15\mathrm{Re}_p{}^{0.687}\right) & \mathrm{Re}_p \leqslant 1000 \\ 0.44 & \mathrm{Re}_p > 1000, \end{cases} \tag{6}$$

where C_D is the drag coefficient dependent on the particle Reynolds number, $\mathrm{Re}_p = \rho_{\mathrm{f}}\varepsilon_{\mathrm{f}}d_p|\boldsymbol{u}_{\mathrm{f}} - \boldsymbol{v}_p|/\mu_{\mathrm{f}}$. Meanwhile, to characterize the overall flow regime in the rotating drum, a global Reynolds number $\mathrm{Re}_{\mathrm{g}} = \rho_{\mathrm{f}}\omega r d_p/\mu_{\mathrm{f}}$ is defined with r being the radius of the cylindrical drum. In addition, the lubrication force is not considered in our simulation. When particles are separated by a lubrication film, both the normal and tangential interparticle stressed could be mediated [35]; however, the fraction of power dissipated by such a mediation is highly sensitively to the ratio of two dimensionless numbers—the inertial number I and the viscous number J [36]. With $I/J = \sqrt{\rho_{\mathrm{s}}P_{\mathrm{s}}}d_{\mathrm{s}}/\mu_{\mathrm{f}}$, where P_{s} is the confining pressure, for the lowest $\omega = 5$ rpm in this study, the mean value of I/J is about 4995 quantified by the continuum simulation for monodisperse phase rotating drum test in our previous study [23]; that is, the corresponding lubrication force is negligible according to Trulsson, Andreotti, and Claudin [36].

For the numerical setup, the drum geometry, particle diameters, and drum filling ratio are consistent with the experimental configurations. The computational cell size in CFD is set to $2d_p$, and the time steps for CFD and DEM are 10^{-3} and 10^{-4} s, respectively, verified by sensitivity studies. To calibrate the model parameters regarding friction and collision, a benchmark simulation is conducted based on the monodispersed granular flows. The angles of repose (θ_m) at different rotating speeds are measured under submerged conditions for three different particle densities. Despite the

use of different materials, $\mu_s = 0.3$ fits the results of all these monodisperse tests with an error less than 0.38%. Therefore, we institutively employed 0.3 for the friction coefficient between different types of grains, since we focus on the decoupled influence of grain and fluid density rather than other material-specific properties. Via this manner, the rolling friction coefficient ($\mu_r = 0.0002$) was also determined by trial and error. In addition, according to the rate and state-dependent law [37], if the state variable associated with the contact aging effect is omitted, the frictional coefficient μ is a function of sliding velocity V, $\mu = \mu_0 + a\ln(V/V_0)$, with μ_0 and V_0 being the quasistatic friction coefficient and the referenced velocity, respectively. In Li, Zhang, Chen, Feng, and Li [37], $a = O(0.1)$ is a constant; this explains why $\mu_s = 0.3$ is higher than those from low-speed or quasistatic experiments, i.e., 0.16 in Tang, Song, Dong, and Song [38] and 0.2 in Pijpers and Slot [39], to realize the high-speed experimental phenomenon. If the grain contact speed is assumed to be the linear speed of the rotating drum, $V = \omega\Delta r$, where Δr is the distance between the point and the center, for a rough estimate, with $V_{\max}/V_{\min} = O(10)$ we achieve that $\mu_{\max} - \mu_{\min} \approx 0.23$ by setting $a = 0.1$ and $V_{\max}/V_{\min} = 10$. If the quasi-static friction coefficient [$\in (0.16, 0.2)$] from the experiment is utilized as $\mu_{\min}$, it is plausible to use the arithmetic mean $\mu_s \approx 0.3$ as the mean-field approximation. All other parameters, like fluid viscosity ($\mu_f = 0.001$ Pa s), Young's modulus, and Poisson's ratio of grains, are kept consistent with experiment. Consequently, $\mu_s = 0.3$, $\mu_r = 0.0002$, and $e = 0.5$.

To quantify the segregation between binary mixtures, Lacey mixing index [15] is applied:

$$M = \frac{\left(\sigma^2 - \sigma_0^2\right)}{\left(\sigma_m^2 - \sigma_0^2\right)} \in [0, 1], \tag{7}$$

with $\sigma^2 = \sum_{i=1}^{N} \frac{(\phi_i - \phi_m)^2}{N-1}$, where N is the number of identical cells occupied by all grains, and ϕ_i and ϕ_m are the local and the mean concentration of tracer grains, respectively; $\sigma_0^2 = \phi_m(1 - \phi_m)$ is the theoretical upper limit, while $\sigma_m^2 = \frac{\sigma_0^2}{n}$, with n being the grain number in the ith cell is the possible minimum value. The grain domains are divided into identical cubic cells of size ℓ, and ϕ_i in each cell is identified as the light particles in binary mixtures. A sensitivity study of M using $\ell = 3d_p, 4d_p, 5d_p$ is presented in Fig. 1(c), showing ℓ has less influence on M in the steady state, which is consistent with a previous study [40]. Based on the numerical accuracy, $\ell = 4d_p$ is adopted for all cases, the spatial structure of grids is shown in the inset of Fig. 1(c). In addition, as shown in the inset of Fig. 2(a) on the mixing index, the numerical and experiment results M_s and M_e have a maximum relative error is 2.8%. Notably, due to the difficulty in quantifying the 3D experimental postmortem M, both M_s and M_e are measured from visible layers close to the cylinder boundaries. In the following, we extend the range of the effective density ratio $\mathcal{D}$ by varying fluid density $\rho_f \in [0.2\rho_w, \rho_w]$ and particle density $\rho_s \in [1.400\rho_w, 9.743\rho_w]$.

III. RESULTS AND DISCUSSIONS

A. Effect of effective density ratio

Experimental observations demonstrate four distinctive mixing patterns of submerged density-disperse systems, as shown in the left column of Fig. 1(b). The well-mixed state is pertinent to that of a dry system. However, the segregation patterns are totally different; that is, the net symmetry of the segregation profiles diminishes as seen from the eccentricity of heavy grains, which is enhanced with ω increasing. Meanwhile, the heavy grains become more clustering and closer to the boundary of the drum, leading to nearly complete segregation. Notably, for the POM-glass mixture ($\mathcal{D} = 1.6$), no matter how high ω is, no visible segregation was encountered, which is against the observations in the POM-steel ($\mathcal{D} = 17$) and the steel-glass ($\mathcal{D} = 5$) mixtures. To gain deeper insights into the segregation transition, especially for the grain scale such as contact number distributions, extra CFD-DEM simulations are conducted to investigate density effects.

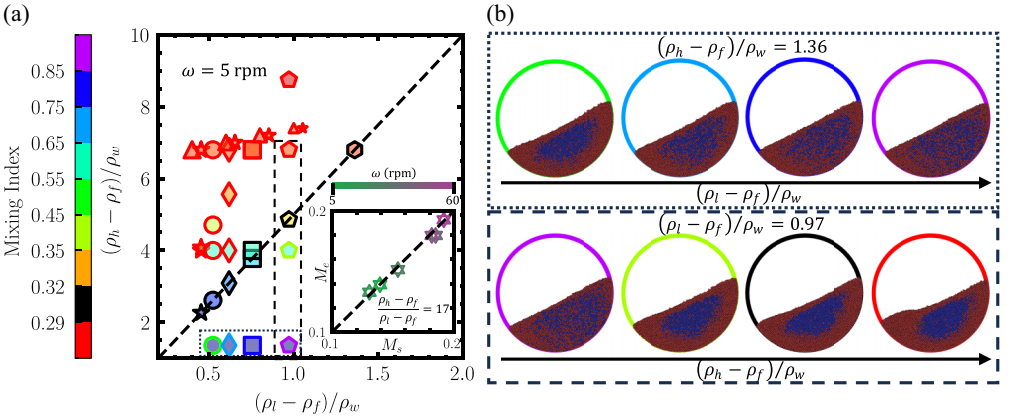

FIG. 2. (a) Phase diagram illustrating the mixing index, M, as in Eq. (7), across various combinations of heavy (ρ_h) and light (ρ_l) particle densities, as well as fluid densities ρ_f, at a fixed rotating speed, $\omega = 5$ rpm. The black dashed line corresponds to $(\rho_\mathrm{h} - \rho_\mathrm{f})/(\rho_\mathrm{l} - \rho_\mathrm{f}) = 5$. The marker edge color represents the values of M, while filled color, shape, and size of the marker indicate values of ρ_h, ρ_l, and ρ_f, respectively, consistent with those in Fig. 3(a). The inset compares the numerical (M_s) and experimental (M_e) mixing indices for submerged steel and POM mixtures with various rotating speeds. (b) Visualisations of specific steady mixing states in (a), in which the outer ring color indicates M value. The red and blue particles represent the lighter and heavier particles, respectively.

Because the segregation patterns are dominated by the gravity and buoyancy forces proportional to the density differences, Fig. 2 shows a phase diagram for M influenced by $\rho_\mathrm{h} - \rho_\mathrm{f}$ and $\rho_\mathrm{l} - \rho_\mathrm{f}$. We define $M \geqslant 0.32$ as the mixed state, and $M < 0.32$ shows segregation with two distinct modes. The regime of $0.29 < M < 0.32$ has been explored previously as the central core segregation mode [6,21], whilst $M \leqslant 0.29$ breaks the symmetry from the previous mode and transits toward nearly complete segregation. As illustrated by data points in the dashed and dotted rectangles for the same ω and ρ_f in Fig. 2(a), of which the steady-state configurations are provided in Fig. 2(b), M is not uniquely dependent on ρ_h or ρ_l, but on the combined effect of the two with the presence of pore fluid. We introduce an effective density ratio $\mathcal{D} = \frac{\rho_\mathrm{h} - \rho_\mathrm{f}}{\rho_\mathrm{l} - \rho_\mathrm{f}}$ to characterize this combined effect. According to our numerical results, for $\mathcal{D} < 5$, the system remains at a well-mixed stage, whereas for $\mathcal{D} \geqslant 5$, nearly complete segregation occurs. The dashed diagonal line in Fig. 2(a) marks the transition states corresponding to $\mathcal{D} = \frac{\rho_\mathrm{h} - \rho_\mathrm{f}}{\rho_\mathrm{l} - \rho_\mathrm{f}} = 5$. However, this transition threshold is arbitrary because the transition is gradual and not strictly defined by $\mathcal{D} = 5$; nonetheless, it is evident that M is strongly influenced by $\mathcal{D}$.

As demonstrated in Fig. 3(a), wherein all numerical realizations in Fig. 2(a) are included, M monotonically decreases with $\mathcal{D}$ following an exponential law, $M = (1-c)e^{b(\mathcal{D}-1)} + c$, with two parameters $b < 0$, and $0 < c < 1$. Considering two extreme cases: monodisperse grain mixtures, for $\rho_\mathrm{h} = \rho_\mathrm{l}$ we have $(\mathcal{D}, M) = (1, 1)$; and for $\rho_\mathrm{l} \to \rho_\mathrm{f}$, $\lim_{\rho_\mathrm{l} \to \rho_\mathrm{f}} \mathcal{D} = +\infty \to \lim_{\rho_\mathrm{l} \to \rho_\mathrm{f}} M = c$, i.e., $(\mathcal{D}, M) = (+\infty, c)$. The parameter c sets the segregation limit in our binary-mixture system, and the actual value depends on the drum conditions, including the geometry, speed, and filling state. The particle-particle interactions often dominate in dense granular flows and that the inertial number $I = \dot{\gamma} d_\mathrm{s}/\sqrt{\rho_\mathrm{s}/p_\mathrm{s}}$ is widely used to characterize local granular flow behaviors. However, $\dot{\gamma}$ and p_s are spatially heterogeneous across the domain in our study, similar to the definition of the local Reynolds number. Herein, the global inertial number $I_\mathrm{g} = \dot{\gamma}/\sqrt{d_\mathrm{s}/(g\cos\theta_m)}$ is defined based on the tests from Govender [41], Orpe and Khakhar [42], and Chou and Lee [43]. The shear rate $\dot{\gamma}$ therein is a function of the combination of the dynamic and quasistatic incline angle of the continuous free surface of monodisperse grains, whilst in our polydisperse grains, no continuous free surface

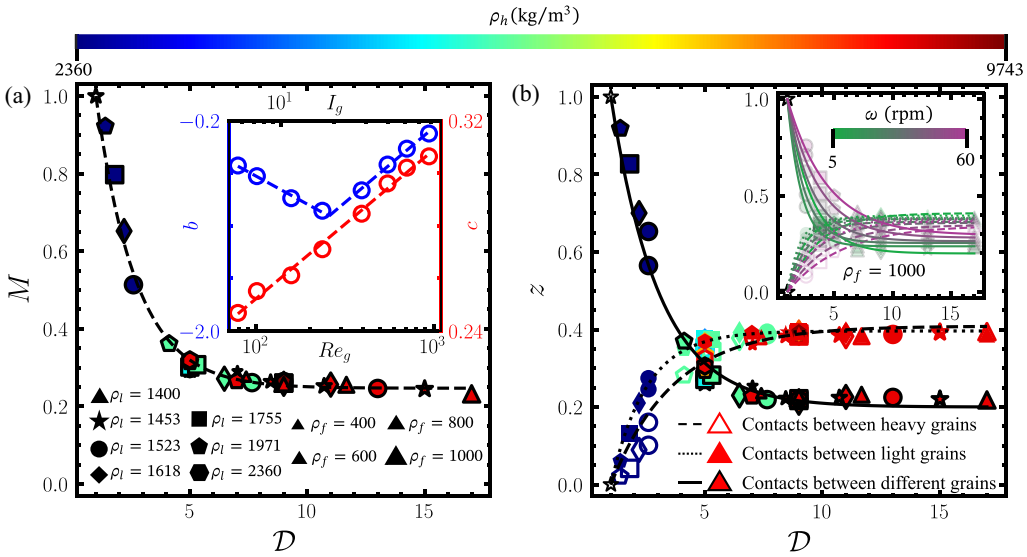

FIG. 3. (a) Mixing-index M as a function of the effective density ratio $\mathcal{D}$ at $\omega = 5$ rpm. Dashed lines indicate the fitted functions, and the hollow pentagram denotes $(\mathcal{D}, M) = (1, 1)$. The inset illustrates the parameters b and c vs $\mathrm{Re_g}$ and I_g. (b) Contact number ratio z plotted against $\mathcal{D}$ at $\omega = 5$ rpm. The upper hollow pentagram is for $(\mathcal{D}, z) = (1, 1)$, while the bottom hollow pentagram is for $(\mathcal{D}, z) = (1, 0)$. The inset is for z versus $\mathcal{D}$ for various rotating speeds.

appears and thus more than one incline angles are encountered in the dynamic regime as shown in Fig. 1. Therefore, $\dot{\gamma} = \omega r/(2\pi r)$ and $\tan\theta_m = \mu_\mathrm{s}$ are selected in I_g. Specific evolutions of b and c with the global Reynolds number and inertial number, $\mathrm{Re_g}$ and I_g, are provided in the inset of Fig. 3(a). Interestingly, c is logarithmically linear to $\mathrm{Re_g}$ and I_g, while b is logarithmically bilinear to $\mathrm{Re_g}$ and I_g, indicating the wet granular flow transition from the viscous- to inertial-dependent regime [44].

Since M is rooted in contact numbers—readily accessible in simulations—of the associated mixtures, to gain deeper insights into how it evolves with $\mathcal{D}$, Fig. 3(b) shows the proportions (z_h, z_l, and z_d) in the total contact number of three contact types, namely contacts between heavy grains, contact between light grains, and contacts between different types of grains. These proportions are defined based on individual particles, classified exclusively into one of the three contact categories. The contact is determined by a distance criterion between any two adjacent particles whose center distance $l \leqslant 1.05d_p$. This criterion is also implemented for the validations in the inset of Fig. 2(a). Interestingly, all three proportions evolve with varying $\mathcal{D}$ in an exponential fashion like M, indicating that the exponential dependence of M on $\mathcal{D}$ can be explained by contact proportion evolutions. Therein, at $\mathcal{D} = 1$, the submerged density disperse system degrades to monodisperse wet mixtures and, thus the two types of particles are perfectly mixed as long as rotating revolutions are enough. This could induce no contact between different types of grains; that is, $z_h = z_l = 0$ and $z_d = 1$. With increased $\mathcal{D}$ while keeping ω consistent, z_h and z_l rise and gradually saturate because of the emergence of complete segregation. Moreover, akin to M, the ω-dependent exponential evolutions with $\mathcal{D}$ are also demonstrated in the inset of Fig. 3(b). When the drum is rotated more rapidly, the wider spatial allocation of both types of grains results in more area of the contact boundary between the heavy grain clusters and its surrounding light grains, as illustrated in the left column of Fig. 1(b). This explains why higher ω contributes to larger z_d. Meanwhile, z_h and z_l have decreased since $z_h + z_l + z_d = 1$.

B. Segregation pattern transitions

From the three experimentally observed segregation patterns in Fig. 1(b)—each exhibiting one, two, or three vortices (the third, typically smaller, forming near the top center of the mixture)—all mixing indices calculated from the corresponding simulation are less than 0.29, but the mixing patterns are totally different. To quantitatively describe such a difference in the nearly complete segregation patterns, we measure the vortex information in them. With both increases of $\mathcal{D}$ and ω, the trajectories depicted in the middle column of Fig. 1(b) reveal a transition from a single-core pattern to two- or three-core pattern, with the counterclockwise motion of the heavy grain cluster parallel to the drum rotating direction. It has been widely observed that, in a dry density disperse system, heavy grains could congregate in the core of the symmetrical mixture [45]. In dry rotating drums, vortex structures commonly arise from granular avalanching dynamics, where surface particles descend under gravity while particles near the base are advected upward by shear induced at the rotating boundary. The interaction between these opposing motions gives rise to convective loops within the granular bulk [10,46]. As a thought experiment, if fluid is introduced into the granular system at steady state, the heavy grain cluster experiences a resultant macroscopic force arising from buoyancy opposing gravity and fluid drag aligned with the local flow velocity. This resultant force tends to relocate the heavy cluster toward a position concurrent with the drum rotation, thereby inducing the observed asymmetric distribution. This asymmetry could be enhanced with rising ω, which induces higher drag forces, as described in Eq. (5). Additionally, at a higher $\mathcal{D}$, light grains behave similar to the surrounding fluid, allowing heavy grains to exhibit independent motions—like a system just for the mixture of heavy grains and fluids—and to get closer to the cylinder boundary. From the view of the fluid motion, as illustrated by the fluid velocity field in Fig. 1(b), at lower $\mathcal{D}$ and ω, a single vortex is formed, with the peak fluid velocity concentrated within the grain region. As $\mathcal{D}$ increases ($\mathcal{D} = 17$), the fluid flow develops a distinct jet-like structure that emerges between the two granular phases, which is spatially decoupled from the dense granular regions and induces the formation of two vortices on either side. At higher ω (=30 rpm), a fluid convection develops within the lighter granular regions. This extended fluid convection leads to the emergence of the third vortex.

Influences of $\mathcal{D}$ and ω on modes of the nearly complete segregation are detangled via vortex number $\mathcal{N}$ and vortex area $\mathcal{A}$. To this end, the codes [47] in the MATLAB® environment for Γ_2 criterion proposed by Graftieaux, Michard, and Grosjean [48] are implemented to identify and measure vortexes. All illustrative visualisations of the three identified vortex configurations are provided in Fig. 1(b). From the phase diagram in Fig. 4(a), dry density disperse system like patterns with one vortex (V_1) in heavy grains could only be attained at low values of both $\mathcal{D}$ and ω. Amplifying $\mathcal{D}$ or ω can induce a second vortex V_2 in light grains. A third vortex V_3, located near the center of the mixture in light grains, could emerge at both high $\mathcal{D}$ and ω. Figure 4(b) shows the combined effect of $\mathcal{D}$ and ω on evolutions of the three vortex areas. For V_1, the vortex area persists regardless of ω at higher $\mathcal{D}$; however, due to the relatively less inertial forces of heavy grains to light grains at lower $\mathcal{D}$, the persistency of $\mathcal{A}_{V_1}$ with varying ω is diminished. This tendency also suits the evolution of $\mathcal{A}_{V_2}$. Compared with $\mathcal{A}_{V_1}$, $\mathcal{A}_{V_2}$ reduces rapidly when $\mathcal{D}$ is decreased, because the movement of lighter grains can fluctuate more and deviate from the stable trace lines forming the vortex. Interestingly, at the extremely low $\mathcal{D} = 5$, $\mathcal{A}_{V_2}$ could be even smaller than $\mathcal{A}_{V_3}$, considering generally we have $\mathcal{A}_{V_1} > \mathcal{A}_{V_2} > \mathcal{A}_{V_3}$.

C. Discussions

The results demonstrate that the CFD-DEM approach accurately reproduces the experimentally observed segregation patterns. At a fixed ω, the mixing efficiency, quantified by the Lacey index M, is controlled primarily by $\mathcal{D}$. This dependence is well-described by an exponential law in which the scaling coefficient c increases monotonically with $\mathrm{Re_g}$, while the $M-\mathcal{D}$ rate factor b transitions from decreasing to increasing at a critical $\mathrm{Re_g}$. Along with these changes in the global scalar fields, the flow undergoes spatially heterogeneous topological bifurcations, marked by the emergence of

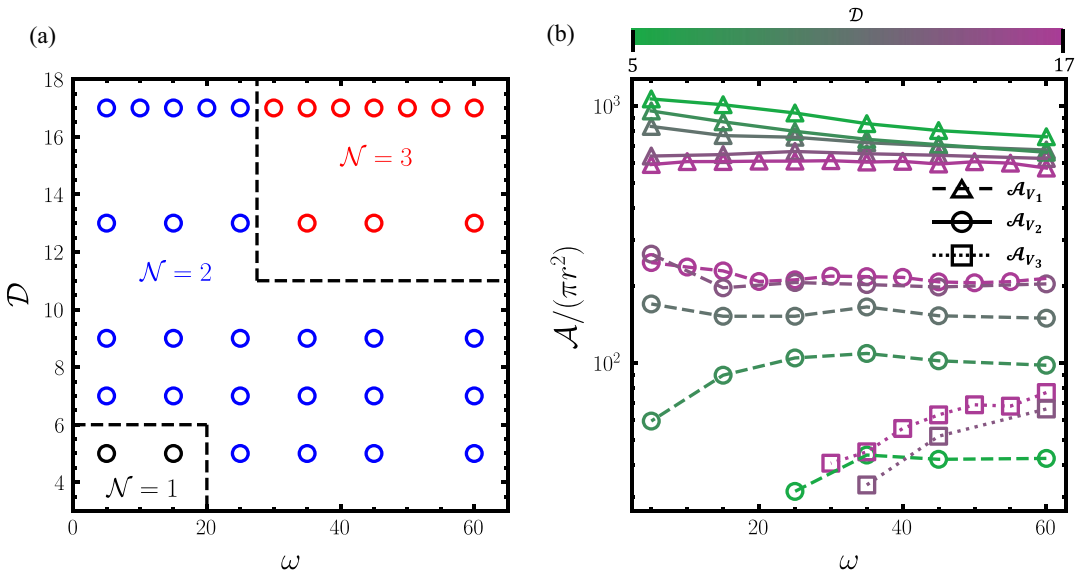

FIG. 4. (a) Phase diagram of the measured number of vortices, $\mathcal{N}$, influenced by the rotating speed ω and the effective density ratio $\mathcal{D}$, as also shown in Fig. 1(b). (b) The normalized vortex area $\mathcal{A}$ by projected area of single grain versus ω, with different $\mathcal{D}$.

multiple coherent vortical structures. Specifically, at low ω and small $\mathcal{D}$, the system exhibits a single focal point of species segregation and drum-relative circulation; however, higher rotation rates or larger density contrasts generate a second core domain in which lighter grains collect and circulate, and a third vortex can eventually form at even higher-density contrasts.

Although the current work systematically explores the effects of $\mathcal{D}$ and ω, the influence of the drum filling fraction—known to induce quasistatic regions in dry systems [49]—has yet to be addressed under submerged conditions with a careful consideration of lubrication force, nor has the impact of drum width and geometry (e.g., circular, elliptical, or polygonal) been fully explored. Moreover, fully characterizing the bilinear change in the coefficient b and clarifying the viscous-inertial transition at the particle scale—particularly the role of the interstitial fluid viscosity and particle-particle interactions—remains essential [36,50]. For instance, it warrants further investigation of linking these transitions to the local Stokes number or other comparable grain-scale metrics, such as the local inertial number in a simplified configuration, although $\mathrm{Re_g}$ is adopted as a system-scale descriptor due to the spatially heterogenous of the local strain rate and pressure. While global measures such as the Lacey index effectively capture overall mixing states, coupling local flow rheology and stress-segregation can potentially pave the way towards enriching and combining the existing scaling theories, such as the submerged grainsize [51] and density segregation frameworks [52].

IV. CONCLUSION

This study provides a comprehensive analysis of density-driven segregation of binary granular mixtures in a rotating drum. The observations from experiments and numerical simulations reveal four distinct mixing states—from well-mixed states to complicated segregation patterns with increasing numbers of vortices. A new factor, the effective density ratio $\mathcal{D}$, is defined to bridge the grain and fluid properties and the macroscopic mixing index M. A new model is also proposed to predict M for a density-disperse system. The nearly complete segregation patterns transformed from the well-mixed state are classified by quantitative analysis of vortices in the two grain phases. The

vortex area and number are highly sensitive to $\mathcal{D}$ and ω. These results extend our understanding of submerged grain segregation, providing critical insights into how to segregate two mixed dry grains by adding specific fluids. The identification of the scaling laws between M and $\mathcal{D}$ contributes to broader science and engineering communities of granular flow, such as geophysics and industrial manufacturing.

ACKNOWLEDGMENTS

D.W. acknowledges financial support by the National Natural Science Foundation of China [the Excellent Young Scientists Fund (overseas)] and by the Australian Research Council [ARC, the Discovery Early Career Award (DECRA), Grant No. DE240101106].

Y.C.: Conceptualizsation, Formal analysis, Methodology, Visualization, Writing original draft, Writing review and editing; D.W.: Conceptualization, Formal analysis, Methodology, Visualization, Supervision, Writing original draft, Writing review and editing; S.S.: Methodology, Writing review and editing; M.D.: Writing review & editing; Y.G.: Conceptualization, Formal analysis, Methodology, Visualization, Supervision, Writing review and editing.

The authors report no conflict of interest.

DATA AVAILABILITY

The data that support the findings of this article are not publicly available. The data are available from the authors upon reasonable request.

[1] R. M. Iverson, The physics of debris flows, Rev. Geophys. **35**, 245 (1997).

[2] B. Ferdowsi, C. P. Ortiz, M. Houssais, and D. J. Jerolmack, River-bed armouring as a granular segregation phenomenon, Nat. Commun. **8**, 1363 (2017).

[3] N. Sommier, P. Porion, P. Evesque, B. Leclerc, P. Tchoreloff, and G. Couarraze, Magnetic resonance imaging investigation of the mixing-segregation process in a pharmaceutical blender, Int. J. Pharm. **222**, 243 (2001).

[4] S. Badar and I. H. Farooqi, Pulp and paper industry—manufacturing process, wastewater generation and treatment, *Environmental Protection Strategies for Sustainable Development* (Springer, Dordrecht, 2012), p. 397.

[5] P. B. Umbanhowar, R. M. Lueptow, and J. M. Ottino, Modeling segregation in granular flows, Annu. Rev. Chem. Biomol. Eng. **10**, 129 (2019).

[6] I. Zuriguel, J. Peixinho, and T. Mullin, Segregation pattern competition in a thin rotating drum, Phys. Rev. E **79**, 051303 (2009).

[7] D. Khakhar, A. V. Orpe, and S. Hajra, Segregation of granular materials in rotating cylinders, Physica A **318**, 129 (2003).

[8] T. Barker, M. Rauter, E. S. F. Maguire, C. G. Johnson, and J. M. N. T. Gray, Coupling rheology and segregation in granular flows, J. Fluid Mech. **909**, A22 (2020).

[9] J. W. Vallance and S. B. Savage, IUTAM symposium on segregation in granular flows, in *Proceedings of the IUTAM Symposium Held in Cape May, NJ, June 5–10, 1999* (Springer, Dordrecht, 2000), p. 31.

[10] J. M. N. T. Gray, Particle segregation in dense granular flows, Annu. Rev. Fluid Mech. **50**, 407 (2018).

[11] Y. Duan, P. B. Umbanhowar, J. M. Ottino, and R. M. Lueptow, Segregation models for density-bidisperse granular flows, Phys. Rev. Fluids **5**, 044301 (2020).

[12] C.-C. Liao, A study of the effect of liquid viscosity on density-driven wet granular segregation in a rotating drum, Powder Technol. **325**, 632 (2018).

[13] C. Sun, T. Mullin, L. Van Wijngaarden, and D. Lohse, Drag and lift forces on a counter-rotating cylinder in rotating flow, J. Fluid Mech. **664**, 150 (2010).

[14] Á. Vergara, D. Wei, and R. Fuentes, Drag coefficient for irregularly shaped grains: Rotational dependence at various Reynolds numbers, J. Fluid Mech. **994**, A1 (2024).
[15] P. M. C. Lacey, Developments in the theory of particle mixing, J. Appl. Chem. **4**, 257 (1954).
[16] G. H. Ristow, Particle mass segregation in a two-dimensional rotating drum, Europhys. Lett. **28**, 97 (1994).
[17] D. Khakhar, J. McCarthy, and J. M. Ottino, Radial segregation of granular mixtures in rotating cylinders, Phys. Fluids **9**, 3600 (1997).
[18] A. Tripathi and D. Khakhar, Density difference-driven segregation in a dense granular flow, J. Fluid Mech. **717**, 643 (2013).
[19] Q. Shi, G. Sun, M. Hou, and K. Lu, Density-driven segregation in vertically vibrated binary granular mixtures, Phys. Rev. E **75**, 061302 (2007).
[20] C. Tai, S. Hsiau, and C. Kruelle, Density segregation in a vertically vibrated granular bed, Powder Technol. **204**, 255 (2010).
[21] C.-C. Liao, M. L. Hunt, and H.-L. Sun, Experimental study on the combined influence of particle shape, density, and size on segregation behavior in binary and ternary granular mixtures, Phys. Fluids **36**, 073315 (2024).
[22] G. G. Pereira, M. D. Sinnott, P. W. Cleary, K. Liffman, G. Metcalfe, and I. D. Šutalo, Insights from simulations into mechanisms for density segregation of granular mixtures in rotating cylinders, Granular Matter **13**, 53 (2010).
[23] Y. Chen, S. Suo, M. Dong, H. Zhong, D. Wei, and Y. Gan, Effects of particle density and fluid properties on mono-dispersed granular flows in a rotating drum, Phys. Fluids **36**, 103324 (2024).
[24] F. Romanò, A. Hajisharifi, and H. C. Kuhlmann, Cellular flow in a partially filled rotating drum: Regular and chaotic advection, J. Fluid Mech. **825**, 631 (2017).
[25] X. Tang, S. Wang, X. Jin, and Y. Shen, Super-quadric CFD-DEM modelling of chip-like particle-liquid flow in a rotary drum, Powder Technol. **435**, 119363 (2024).
[26] M. Arntz, H. Beeftink, W. K. den Otter, W. J. Briels, and R. Boom, Segregation of granular particles by mass, radius, and density in a horizontal rotating drum, AlChE J. **60**, 50 (2014).
[27] K. Hill, A. Caprihan, and J. Kakalios, Axial segregation of granular media rotated in a drum mixer: Pattern evolution, Phys. Rev. E **56**, 4386 (1997).
[28] G. Seiden and P. J. Thomas, Complexity, segregation, and pattern formation in rotating-drum flows, Rev. Mod. Phys. **83**, 1323 (2011).
[29] See Supplemental Material at http://link.aps.org/supplemental/10.1103/kjhc-9chw for experimental and numerical videos of segregation patterns.
[30] Y. Tsuji, T. Kawaguchi, and T. Tanaka, Discrete particle simulation of two-dimensional fluidized bed, Powder Technol. **77**, 79 (1993).
[31] Z. Zhou, S. Kuang, K. Chu, and A. Yu, Discrete particle simulation of particle–fluid flow: Model formulations and their applicability, J. Fluid Mech. **661**, 482 (2010).
[32] P. A. Cundall and O. D. Strack, A discrete numerical model for granular assemblies, Geotechnique **29**, 47 (1979).
[33] N. V. Brilliantov, F. Spahn, J.-M. Hertzsch, and T. Pöschel, Model for collisions in granular gases, Phys. Rev. E **53**, 5382 (1996).
[34] D. Gidaspow, *Multiphase Flow and Fluidization: Continuum and Kinetic Theory Descriptions* (Academic Press, San Diego, 1994).
[35] R. Cox, The motion of suspended particles almost in contact, Int. J. Multiphase Flow **1**, 343 (1974).
[36] M. Trulsson, B. Andreotti, and P. Claudin, Transition from the viscous to inertial regime in dense suspensions, Phys. Rev. Lett. **109**, 118305 (2012).
[37] S. Li, S. Zhang, Z. Chen, X.-Q. Feng, and Q. Li, Length scale effect in frictional aging of silica contacts, Phys. Rev. Lett. **125**, 215502 (2020).
[38] H. Tang, R. Song, Y. Dong, and X. Song, Measurement of restitution and friction coefficients for granular particles and discrete element simulation for the tests of glass beads, Materials **12**, 3170 (2019).

[39] R. J. M. Pijpers and H. M. Slot, Friction coefficients for steel to steel contact surfaces in air and seawater, J. Phys.: Conf. Ser. **1669**, 012002 (2020).
[40] X. Jin, G. R. Chandratilleke, S. Wang, and Y. Shen, DEM investigation of mixing indices in a ribbon mixer, Particuology **60**, 37 (2022).
[41] I. Govender, Granular flows in rotating drums: A rheological perspective, Miner. Eng. **92**, 168 (2016).
[42] A. V. Orpe and D. Khakhar, Rheology of surface granular flows, J. Fluid Mech. **571**, 1 (2007).
[43] H.-T. Chou and C.-F. Lee, Cross-sectional and axial flow characteristics of dry granular material in rotating drums, Granular Matter **11**, 13 (2008).
[44] V. Topin, Y. Monerie, F. Perales, and F. Radjai, Collapse dynamics and runout of dense granular materials in a fluid, Phys. Rev. Lett. **109**, 188001 (2012).
[45] K. Hill, D. Khakhar, J. Gilchrist, J. McCarthy, and J. Ottino, Segregation-driven organization in chaotic granular flows, Proc. Natl. Acad. Sci. USA **96**, 11701 (1999).
[46] S. González, C. Windows-Yule, S. Luding, D. Parker, and A. R. Thornton, Forced axial segregation in axially inhomogeneous rotating systems, Phys. Rev. E **92**, 022202 (2015).
[47] S. Endrikat, Find vortices in velocity fields, MATLAB Central File Exchange. Retrieved October 30, 2024, https://www.mathworks.com/matlabcentral/fileexchange/52343-find-vortices-in-velocity-fields.
[48] L. Graftieaux, M. Michard, and N. Grosjean, Combining PIV, POD and vortex identification algorithms for the study of unsteady turbulent swirling flows, Meas. Sci. Technol. **12**, 1422 (2001).
[49] E. Maguire, T. Barker, M. Rauter, C. Johnson, and J. Gray, Particle-size segregation patterns in a partially filled triangular rotating drum, J. Fluid Mech. **979**, A40 (2024).
[50] K. F. E. Cui, G. G. D. Zhou, and L. Jing, Particle segregation and diffusion in fluid-saturated granular shear flows, Phys. Rev. Fluids **7**, 014305 (2022).
[51] T. Trewhela, C. Ancey, and J. M. N. T. Gray, An experimental scaling law for particle-size segregation in dense granular flows, J. Fluid Mech. **916**, A55 (2021).
[52] J. M. N. T. Gray and C. Ancey, Particle-size and -density segregation in granular free-surface flows, J. Fluid Mech. **779**, 622 (2015).